Nonlinear dynamics of doped semiconductor quantum dot lasers

K. Lüdge and E. Schöll

Regular Article

Nonlinear dynamics of doped semiconductor quantum dot lasers

K. Lüdge[a] and E. Schöll

Institut für Theoretische Physik, Technische Universität Berlin, Hardenbergstr. 36, 10623 Berlin, Germany

Abstract. We discuss the influence of wetting layer doping on the turn-on dynamics of a quantum dot (QD) laser by using a microscopically based rate equation model which separately treats the dynamics of electrons and holes. As the carrier-carrier scattering rates depend nonlinearly on the wetting layer carrier densities we observe drastic changes of relaxation oscillation frequency and damping if the wetting layer is doped. We gain insight into the nonlinear dynamics of the QD laser by a detailed analysis of various sections of the five-dimensional phase space focusing on changes in the coupling between QD electron and holes dynamics.

1 Introduction

As a result of their unique properties like low threshold current, low bit-error rate, and large temperature stability, quantum dot (QD) lasers constitute an important opto-electronic application of self-organized semiconductor QD structures [1,2]. It has recently been suggested to use a p-doped wetting layer (WL) to improve the performance of the device [3]. In previous works [4–7] it was shown that the nonlinear dynamic response of QD lasers can be quantitatively understood by including the strongly non-linear character of electron-electron scattering processes between the QDs and the two-dimensional WL [8] in a rate equation model. This has also been applied to QD lasers with optical feedback [9]. Here we extent the model in order to describe the effect of doping on the optical output as well as on the internal dynamics of the carriers inside the device.

As a distinguishing feature compared to other rate equation models that include scattering rates which are linear in the WL carrier density and equal for electrons and holes [10–15], we emphasize the importance of different nonlinear rates for both types of carriers with respect to the internal laser dynamics. Following a dynamic hierarchy, our model bridges the gap between a fully microscopic description including polarization and population dynamics [16–19] and rate equations with constant coefficients [20]. Our microscopic calculation of the scattering rates enables a quantitative modeling of the QD laser output without assuming fit parameters for the carrier lifetimes. The effect of inhomogeneous broadening, as discussed in [10,21,22], which was shown to be important in order to discuss the linewidth enhancement factor [12] or mode locking effects [23], is taken into account in a simplified approach which distinguishes only between the

total QD density and the density of the lasing subgroup of QDs whose size matches with the laser mode.

The paper is organized as follows: after introducing the QD laser model in Section 2, we discuss the impact of the band structure on the microscopic scattering rates in Section 3. Subsequently, in Section 4, the impact of WL doping on the laser turn-on dynamics is discussed, before concluding in Section 5.

2 Quantum dot laser model

The analytic and numeric investigations of the laser turn-on dynamics presented here are based on the model given in reference [7]. In the QD laser system the electrons are first injected into the WL before they are captured by the QDs. We consider a two-level system for electrons and holes in the QDs with an energy separation of $\hbar\omega = 0.96$ eV as common for self-organized quantum dots in the InAs/InGaAs material system.

$$\dot{n}_e = S_e^{in} N^{QD} - \frac{1}{\tau_e} n_e - R_{ind}(n_e, n_h, n_{ph}) - R_{sp}(n_e, n_h) \tag{1}$$

$$\dot{n}_h = S_h^{in} N^{QD} - \frac{1}{\tau_h} n_h - R_{ind}(n_e, n_h, n_{ph}) - R_{sp}(n_e, n_h) \tag{2}$$

$$\dot{w}_e = \eta \frac{j(t)}{e_o} + \frac{n_e}{\tau_e} \frac{N^{sum}}{N^{QD}} - S_e^{in} N^{sum} - \tilde{R}_{sp}(w_e, w_h) \tag{3}$$

$$\dot{w}_h = \eta \frac{j(t)}{e_o} + \frac{n_h}{\tau_h} \frac{N^{sum}}{N^{QD}} - S_h^{in} N^{sum} - \tilde{R}_{sp}(w_e, w_h) \tag{4}$$

$$\dot{n}_{ph} = -2\kappa n_{ph} + \Gamma R_{ind}(n_e, n_h, n_{ph}) + \beta R_{sp}(n_e, n_h). \tag{5}$$

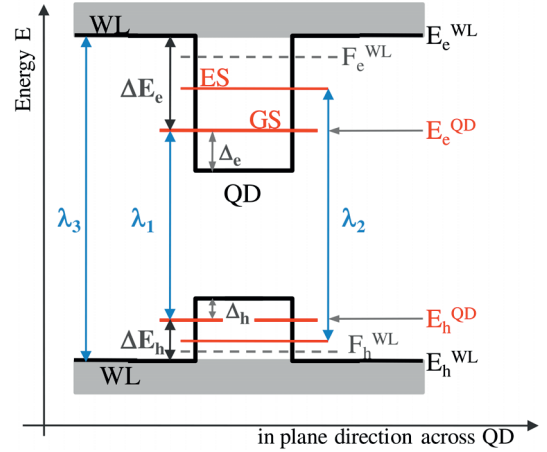The nonlinear rate equations (1)−(5) describe the dynamics of the charge carrier densities in the QDs, n_e and

[a] e-mail: luedge@physik.tu-berlin.de

Table 1. Numerical parameters used in the simulation unless stated otherwise.

Symbol	Value	Symbol	Value
W	$0.7\ \text{ns}^{-1}$	A	$4 \times 10^{-5}\ \text{cm}^2$
T	300 K	N^{QD}	$0.6 \times 10^{10}\ \text{cm}^{-2}$
2κ	$0.1\ \text{ps}^{-1}$	N^{sum}	$20 \times 10^{10}\ \text{cm}^{-2}$
Γ_g	0.075	N^{WL}	$2 \times 10^{13}\ \text{cm}^{-2}$
Γ	2.25×10^{-3}	B^S	$500\ \text{ns}^{-1}\ \text{nm}^2$
μ	$0.75\ e_0\ \text{nm}$	β	5×10^{-6}
ε_{bg}	14.2	$m_e\ (m_h)$	$0.043\ (0.45)m_0$
ΔE_e	210 meV	ΔE_h	50 meV
Δ_e	64 meV	Δ_h	6 meV

Fig. 1. (Color online) Energy diagram of the band structure in the in-plane direction across a QD. The wavelengths λ_1, λ_2 and λ_3 label the optical transitions for ground state (GS), excited state (ES), and WL-state lasing; F_e^{WL} and F_h^{WL} mark the quasi-Fermi levels for electrons and holes, respectively in the WL; E_e^{QD} and E_h^{QD} mark the confined energy of electrons and holes, respectively in the GS of the QD.

n_h, the carrier densities in the WL, w_e and w_h (e and h stands for electrons and holes, respectively), and the photon density n_{ph}. The induced processes of absorption and emission are modeled by a linear gain $R_{ind}(n_e, n_h, n_{ph}) = WA(n_e + n_h - N^{QD})n_{ph}$, where N^{QD} denotes twice the QD density of the lasing subgroup (the factor of 2 accounts for spin degeneracy), $W = \frac{|\mu|^2 \sqrt{\varepsilon_{bg}}}{3\pi\,\varepsilon_0\,\hbar}\left(\frac{\omega}{c}\right)^3$ is the Einstein coefficient and A is the in-plane area of the WL. Analogously to a simple two-level system our model yields positive gain if the occupation probability $f_e^C = n_e/N^{QD}$ of electrons in the localized conduction band level at energy E_e^{QD} is higher than the occupation probability f_e^V of electrons in the localized valence band level at energy E_h^{QD}. The occupation probability of holes in the localized valence band level is given by $f_h^V = 1 - f_e^V = n_h/N^{QD}$. Thus our gain term $R_{ind} = WAN^{QD}(f_e^C - f_e^V)n_{ph} = WAN^{QD}(f_e^C(1 - f_e^V) - f_e^V(1 - f_e^C))n_{ph}$ corresponds to the standard net rate of stimulated emission minus absorption [24].

The spontaneous emission in the QDs is approximated by $R_{sp}(n_e, n_h) = (W/N^{QD})n_e n_h$. The WL spontaneous recombination rate is expressed by $\tilde{R}_{sp}(w_e, w_h) = B^S w_e w_h$ where B^S is the band-band recombination coefficient in the WL. The density N^{sum} is twice the total QD density as given by experimental surface imaging. β is the spontaneous emission coefficient and $\Gamma = \Gamma_g N^{QD}/N^{sum}$ is the optical confinement factor. Γ is the product of the geometric confinement factor Γ_g (i.e. the ratio of the volume of all QDs and the mode volume) and the ratio N^{QD}/N^{sum} (accounting for reduced gain because, due to the size distribution of the QDs, only a subgroup of all QDs match the mode energy for lasing). The coefficient 2κ expresses the total cavity loss, j is the injection current density, e_o is the elementary charge, and $\eta = 1 - w_e/N^{WL}$ is the current injection efficiency that accounts for the fact that we cannot inject any more carriers if the WL is already filled ($w_e = N^{WL}$). The spectral properties of the laser output are not addressed in the model, as the photon density is an average over all longitudinal modes. Changes in the QD size distribution are only taken into account by changes in the active QD density which basically changes the gain. The values of parameters used in our simulations are those listed in Table 1 if not stated otherwise.

3 Microscopic modeling

The dynamics of the QD laser is strongly influenced by the non-radiative carrier-carrier scattering rates S_e^{in} and S_h^{in} for electron and hole capture into the QD levels and S_e^{out} and S_h^{out} for carrier escape from the QD levels, respectively. The resulting scattering times $\tau_e = (S_e^{in} + S_e^{out})^{-1}$ and $\tau_h = (S_h^{in} + S_h^{out})^{-1}$ determine the timescales for changes in the carrier densities. The scattering rates are calculated microscopically within the Boltzmann equation and orthogonalized plane wave approach [5]. All electron-electron, hole-hole and mixed electron-hole Auger processes are included in the rates [6]. The Coulomb interaction is considered up to the second order in the screened Coulomb potential. The calculated scattering rates depend in a strongly nonlinear way upon the WL carrier densities w_e and w_h [7].

The energy diagram of the QD laser structure along the in-plane direction is shown in Figure 1. As already discussed in [7], due to the principle of detailed balance, the ratio between in- and out scattering rates for the electrons and holes S_b^{in}/S_b^{out} ($b = e, h$) depends on the energy difference between the QD levels (E_e^{QD} and E_h^{QD}) and the quasi-Fermi levels in the WL (F_e^{WL} and F_h^{WL}). The latter can be expressed by the WL carrier densities (w_e and w_h) and the WL band edges (E_e^{WL} and E_h^{WL}):

$$F_e^{WL}(w_e) = E_e^{WL} + kT \ln\left[\exp\left(\frac{w_e}{\rho_e kT}\right) - 1\right] \quad (6)$$

$$F_h^{WL}(w_h) = E_h^{WL} - kT \ln\left[\exp\left(\frac{w_h}{\rho_h kT}\right) - 1\right] \quad (7)$$

where $\rho_b = m_b/(\pi\hbar^2)$ are the 2D densities of states, m_b are the effective masses of electrons ($b = e$) and holes ($b = h$), respectively, and T is the temperature. Introducing
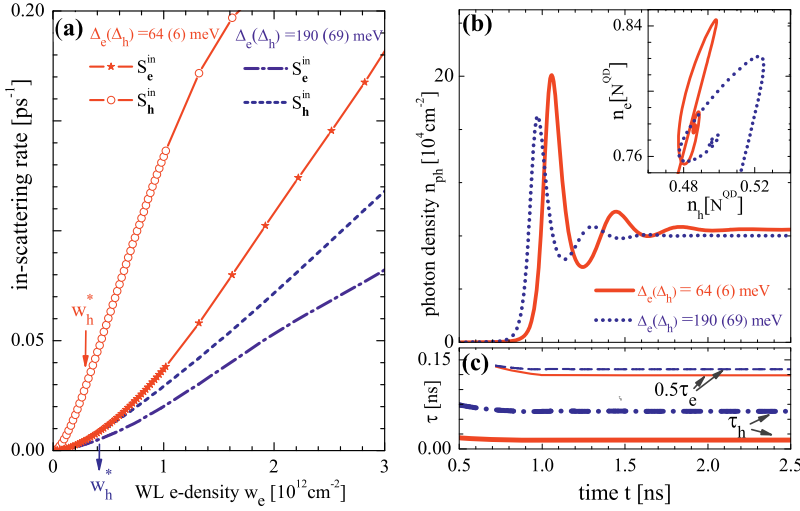
Fig. 2. (Color online) Effect of different zero point energies $\Delta_e = 64$ meV, $\Delta_h = 6$ meV (red solid lines) and $\Delta_e = 190$ meV, $\Delta_h = 70$ meV (dotted blue lines) upon (a) the carrier in-scattering rates $S_{e/h}^{in}(w_e, w_h)$ (for $w_e = w_h$) as a function of the WL e-density w_e and (b) the turn-on transient (inset: turn-on dynamics projected onto the (n_h, n_e)-phase plane); (c) electron and hole scattering times τ_e (thin) and τ_h (thick) as a function of time during the laser turn-on of (b). (Calculated for fixed confinement energies $\Delta E_e = 190$ meV, $\Delta E_h = 70$ meV, $j = 2.5\, j_{th}$, undoped WL)

$\Delta E_e = E_e^{WL} - E_e^{QD}$ and $\Delta E_h = E_h^{QD} - E_h^{WL}$, we can write the ratio between in- and out scattering rates in the following form:

$$S_b^{in}(w_e, w_h) = S_b^{out}(w_e, w_h) e^{\frac{\Delta E_b}{kT}} \left[e^{\frac{w_b}{\rho_b kT}} - 1 \right] \quad (8)$$

where $\rho_b kT$ is the carrier degeneracy concentration ($b = e, h$). The sum $\Delta E_h + \Delta E_e$ can be determined from photoluminescence experiments that measure the wavelength of the ground state emission of the QD (λ_1) and the wavelength of the WL emission (λ_3), as indicated in Figure 1. However, the ratio of electron and hole confinement energies $\Delta E_e / \Delta E_h$ is given by details of the heterostructure and is not known a priori. Thus, later on we will investigate the effect of varying the ratio $\Delta E_e / \Delta E_h$ on the turn-on dynamics of the QD laser.

3.1 Zero point energy

Besides the energy separation ΔE_e and ΔE_h, the scattering rates also depend on the energetic position of the QD ground state with respect to the bottom of the QD potential well indicated as Δ_e and Δ_h in Figure 1. The reason is that this parameter enters as the oscillator strength into the wavefunctions of the confined electrons. For a lens-shaped QD the potential can be approximated by a 2D harmonic oscillator wave function [8] where the zero point energy is exactly the energy spacing between the first excited state (ES) and the ground state (GS). For the QD laser described here experimental data of amplified spontaneous emission [25] suggest an energy spacing $\Delta_e + \Delta_h = 70$ meV between ES and GS emission (λ_2 and λ_1, respectively, see Fig. 1). In contrast to the ratio $\Delta E_h / \Delta E_e$ discussed earlier, the ratio Δ_e / Δ_h is solely given by the ratio of the effective masses of electrons and holes which is $m_h / m_e = 0.45/0.043 = 10.5$ in our simulations.

Different values of Δ_e and Δ_h do not change the detailed balance between electron or hole in- and out scattering (given by Eq. (8)), but they change the ratio between

electron and hole in-scattering rates which is shown in Figure 2a for two different sets of Δ_e and Δ_h. It is obvious that the lower Δ_e is chosen, the higher is the corresponding in-scattering rate. The variation of the scattering rates leads to a changed damping of the laser turn-on as can be seen in Figure 2b where the turn-on transients for the two sets of scattering rates shown in Figure 2a are plotted. For $\Delta_e = 64$ meV, $\Delta_h = 6$ meV (shown in red) the damping is reduced because the ratio between the scattering times $\tau_h / \tau_e \approx 1/16$ is smaller than for the case of $\Delta_e = 190$ meV, $\Delta_h = 70$ meV where $\tau_h / \tau_e \approx 1/4$. The time dependent scattering times τ_e and τ_h during the laser turn-on are plotted in Figure 2c. The steady state carrier densities in the QDs (n_e^* and n_h^*) are only slightly changed if the zero point energy are varied as can be seen in the inset of Figure 2b where the turn-on dynamics is projected onto the (n_h, n_e)-phase plane. This is due to the fact that the steady state values are mainly determined by $\tau_e S_e^{in}$ and $\tau_h S_h^{in}$ which do not depend on the zero point energy. Nevertheless electron and hole dynamics in the QDs are more decoupled (squeezed spiral because of fast hole dynamics) for the case of the lower ratio τ_h / τ_e obtained for $\Delta_e = 64$ meV, $\Delta_h = 6$ meV, see inset of Figure 2b.
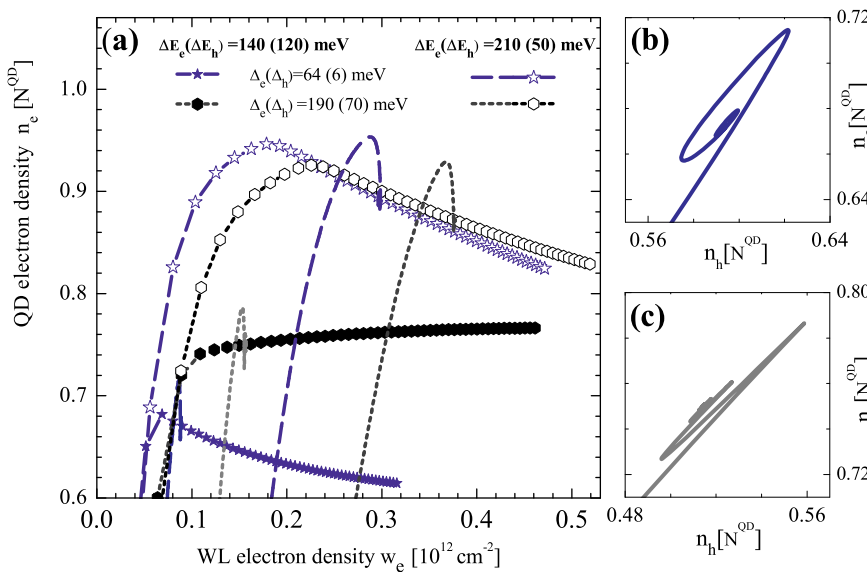
3.2 Confinement energy

As discussed before, the sum of the confinement energies $\Delta E_h + \Delta E_e$ can be measured, while the ratio $\Delta E_h / \Delta E_e$ depends on details of the heterostructure. Changing the ratio $\Delta E_h / \Delta E_e$ results in different scattering rates as well as in different ratios between in- and out-scattering rates S_b^{in} / S_b^{out} (see Eq. (8)). This leads to different products $\tau_e S_e^{in}$ and $\tau_h S_h^{in}$ and therefore to changed steady state values of the carrier densities. Thus the changes observed in the turn-on transients will be much more pronounced than those observed when changing the oscillator strength (and thus the QD size) in the previous section. Figure 3a shows the electron and hole in-scattering rates for $\Delta E_e = 140$ meV, $\Delta E_h = 120$ meV (red solid lines) and $\Delta E_e = 210$ meV, $\Delta E_h = 50$ meV (dotted blue lines).
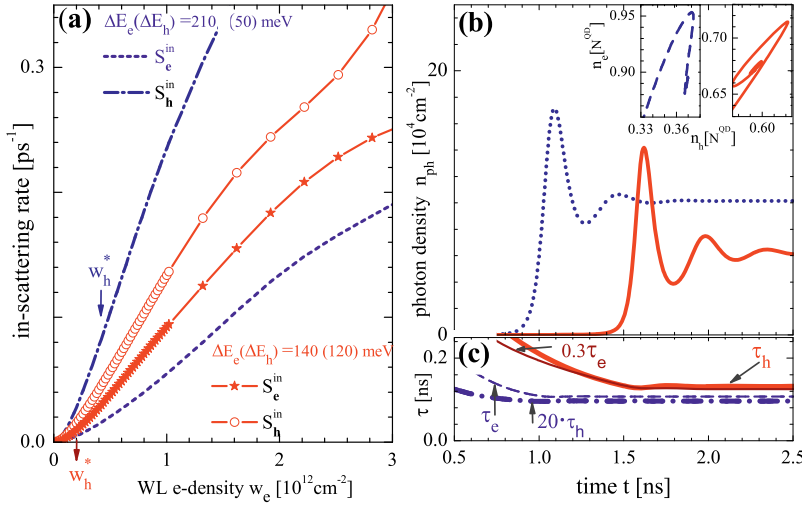
Fig. 3. (Color online) Effect of varying confinement energies $\Delta E_e = 140$ meV, $\Delta E_h = 120$ meV (red solid lines) and $\Delta E_e = 210$ meV, $\Delta E_h = 50$ meV (broken blue lines) upon (a) the carrier in-scattering rates $S_{e/h}^{in}(w_e, w_h)$ (for $w_e = w_h$) as a function of the WL e-density w_e and (b) the turn-on transient (inset: turn-on dynamics projected onto the (n_h, n_e)-phase plane); (c) electron and hole scattering times τ_e (thin) and τ_h (thick) as a function of time during the laser turn-on of (b). (Calculated for fixed $\Delta_e = 64$ meV, $\Delta_h = 6$ meV, $j = 2.5\,j_{th}$, undoped WL.)
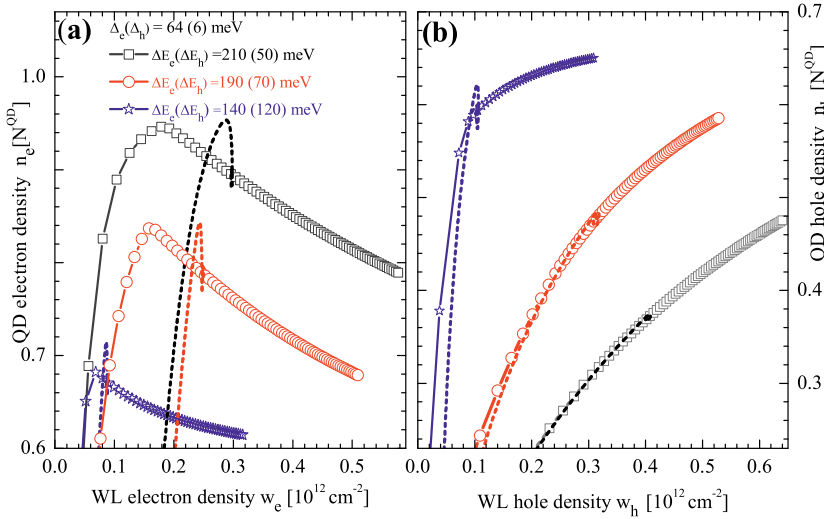
Fig. 4. (Color online) Effect of confinement energy: steady state characteristics for injection currents increasing from $j = 0$ to $j/e_0 = 3 \times 10^9$ cm^{-2} (symbols) and turn-on trajectories for $j = 2.5\,j_{th}$ (dotted lines) projected to the (a) (w_e, n_e)-phase space and (b) (w_e, n_h)-phase space for three different values of the confinement energies: black squares, red circles and blue stars correspond to $\Delta E_e = 210$ meV, $\Delta E_e = 190$ meV, and $\Delta E_e = 140$ meV, respectively with $\Delta E_e + \Delta E_h = 270$ meV (note: threshold current j_{th} changes with ΔE_e) at fixed $\Delta_e = 64$ meV, $\Delta_h = 6$ meV (undoped WL).

Fig. 5. (Color online) Effect of confinement energy and zero point energy: (a) steady state characteristics for $\Delta E_e = 140$ meV, $\Delta E_h = 120$ meV (filled symbols) and $\Delta E_e = 210$ meV, $\Delta E_h = 50$ meV (open symbols) projected onto the (w_e, n_e)-phase space for zero point energies $\Delta_e = 64$ meV, $\Delta_h = 6$ meV (dashed blue lines with stars) and $\Delta_e = 190$ meV, $\Delta_h = 70$ meV (dotted black lines with circles) for injection current increasing from $j = 0$ to $j/e_0 = 2 \times 10^9$ cm^{-2}; dotted and dashed lines are the respective turn-on trajectories for $j = 2.5\,j_{th}$ (Note: threshold current j_{th} changes with ΔE_e and Δ_e); (b) turn-on dynamics projected onto (n_h, n_e)-phase space for $\Delta E_e = 140$ meV, $\Delta E_h = 120$ meV and $\Delta_e = 64$ meV, $\Delta_h = 6$ meV; (c) same as (b) but with $\Delta_e = 190$ meV, $\Delta_h = 70$ meV ($j = 2.5\,j_{th}$, undoped WL).

It can be seen that for the first case the electron in-scattering is only slightly smaller than that for the holes while the difference is much larger for the second case. The turn-on transients for both cases are plotted in Figure 3b. They show an increased damping of the relaxation oscillations for the second case. Figure 3c depicts the time dependent scattering times during the two laser turn-on scenarios shown in Figure 3b. It can be seen that $\tau_h/\tau_e \approx 0.3$ for the first case $\Delta E_e = 140$ meV, $\Delta E_h = 120$ meV (red solid lines refer to $0.3\tau_e$ and τ_h), while it is less than $1/20$ for $\Delta E_e = 210$ meV, $\Delta E_h = 50$ meV (dashed and dash-dotted blue line depict τ_e and $20\tau_h$, respectively). Thus the higher damping cannot be explained by just discussing the ratio τ_h/τ_e as was done in Section 3.1. Instead the variation of the damping is dominantly related to the variation of the products $\tau_e S_e^{in}$ and $\tau_h S_h^{in}$ and thus the variations of the steady state carrier densities. The insets in Figure 3b show the phase space projection of the laser turn-on onto the (n_h, n_e) plane for both cases discussed so far. With increasing ΔE_e the electron out-scattering becomes more and more unlikely thus $\tau_e S_e^{in} \approx 1$ and the steady state value n_e^* approaches N^{QD} which leads to the highly damped relaxation oscillations. For the lower value of $\Delta E_e = 140$ meV the spiral of the turn-on dynamics in the (n_h, n_e)-phase plane is found at $n_e^* \approx n_h^* \approx 0.6\,N^{QD}$ and shows equal dynamics for electrons and holes (besides a phase shift that leads to the spiral). For the second case $\Delta E_e = 210$ meV, $\Delta E_h = 50$ meV the phase space projection onto the (n_h, n_e) plane is not a spiral. This results from the fact that the scattering time of the holes $\tau_h = 5$ ps is much smaller than that for the electrons $\tau_e = 100$ ps, and thus the hole dynamics can be adiabatically eliminated as $n_h(t)$ does not change significantly during the relaxation oscillations.

So far the turn-on dynamics was considered for fixed pump current $j = 2.5\,j_{th}$, where j_{th} denotes the threshold current density. In Figure 4a we show the steady state values of the QD and WL electron density n_e^* and w_e^*, respectively, for increasing pump currents (each symbol in Figure 4a corresponds to a different pump current) for three different sets of confinement energies ΔE_e and ΔE_h. Additionally the turn-on trajectories for fixed pump current $j = 2.5\,j_{th}$ are plotted in the (w_e, n_e)-plane. It can be seen that the steady state electron density n_e^* linearly decreases with w_e^* above the laser threshold, as analytically described in [7]. It is reduced by a reduction of the confinement energy ΔE_e. As the value for the total carrier density at threshold $n_{th} = n_e^* + n_h^* = \frac{2\kappa}{\Gamma W A} + N^{QD}$ does not depend on the scattering rates a reduction of n_e^* is accompanied by an increase of n_h^*. This can be seen in Figure 4b that shows the same data as Figure 4a but projected onto the (w_e, n_h)-phase space. For $\Delta E_e = 140$ meV, $\Delta E_h = 120$ meV the QD electron and hole levels are approximately equally populated. The trajectories for $j = 2.5\,j_{th}$ show that a reduction of ΔE_e is also accompanied by a reduction of the steady state WL carrier density w_e^*.

Figure 5a shows again the steady state values n_e^* and w_e^* as in Figure 4, but this time we add the comparison of

different zero point energies. We already discussed that for $\Delta E_e = 140$ meV, $\Delta E_h = 120$ meV the scattering times for electrons and holes are of the same order of magnitude. By further changing Δ_e and Δ_h, we can find a configuration where the electron and hole dynamics is completely synchronized. This can be seen in the (n_h, n_e)-projection of Figure 5c where a zero point energy of $\Delta_e = 190$ meV, $\Delta_h = 70$ meV is chosen and the spiral disappears. We also obtain completely flat steady state characteristics in the (w_e, n_e)-plane for this case (black dots in Fig. 5a). Changing the zero point energy for a confinement energy of $\Delta E_e = 210$ meV, $\Delta E_h = 50$ meV (solid lines in Fig. 5a) has only a marginal effect on the turn-on dynamics because of the large difference between electron and hole scattering times (Fig. 3c).

4 Doped wetting layer

One way of changing the confinement energies ΔE_e, ΔE_h that enter the microscopic calculations of the scattering rates would be doping the WL, since space charges will lead to band bending and deform the energy scheme. However, doping of the WL will also change the charge conservation condition, which enters into the rate equation system via the initial conditions of the carrier densities. A doped WL can be implemented by choosing different initial conditions for electron and hole densities in the WL. Without doping, initial conditions $n_e^0 = 0$, $n_h^0 = 0$, $w_e^0 = 10^{-2}\rho_e kT$, and $w_h^0 = 10^{-2}\rho_e kT$ have been used. Note that charge conservation is contained in the 5-variable rate equation system, thus leading to only 4 free dynamic variables that are related by:

$$N^{sum}(\dot{n}_e - \dot{n}_h) - N^{QD}(\dot{w}_h - \dot{w}_e) = 0 \qquad (9)$$

which can be integrated giving

$$N^{sum}(n_e - n_h) - N^{QD}(w_h - w_e) = N^{QD}(w_e^0 - w_h^0). \quad (10)$$

By increasing w_e^0 or w_h^0 and keeping the other at the small value of $10^{-2}\rho_e kT$ we are able to model n- or p-doping, respectively. Because the rate equation system treats 2D densities, also the doping concentrations $n \approx w_e^0$ and $p \approx w_h^0$ are given per area. To compare this to 3D doping densities these have to be divided by the WL height which is $h = 4$ nm. Thus $n = 2 \times 10^{11} \text{cm}^{-2}$ corresponds to $n_{3D} = 5 \times 10^{17}$ cm^{-3}. Figure 6 shows that changes in initial conditions drastically modify the QD laser turn-on dynamics. For n-doping the damping of the relaxation oscillations is increased while the damping is drastically reduced if p-doping is introduced. We can understand this behavior by discussing the laser turn-on dynamics as well as the steady state characteristics in the (w_e, n_e) phase space projection. This is done in Figure 7a for 2 different n-doping densities (red squares and triangles) and 2 different p-doping densities (blue circles and asterisks). It can be seen by comparison with the undoped case (black balls) that the n-doping increases the steady state value of the QD electron density n_e^* and w_e^*, while the p-doping
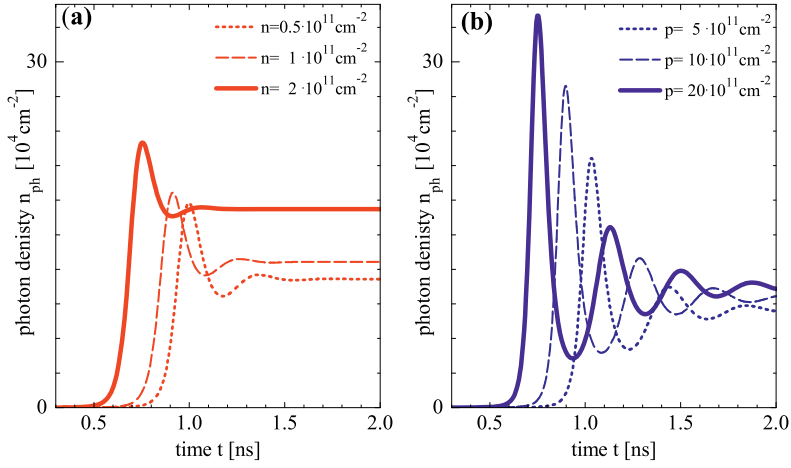
Fig. 6. (Color online) Time series of the photon density during laser turn-on for (a) different n-doping density and (b) different p-doping density. Dotted, dashed and solid lines correspond to doping of 0.1, 0.2 and 0.4 times the degeneracy concentration $\rho_{e/h}kT$, respectively. $\rho_e kT = 4.7 \times 10^{11}$ cm^{-2} and $\rho_h kT = 48 \times 10^{11}$ cm^{-2}. Parameters as in Table 1; pump current is $j = 2.5\,j_{th}$.
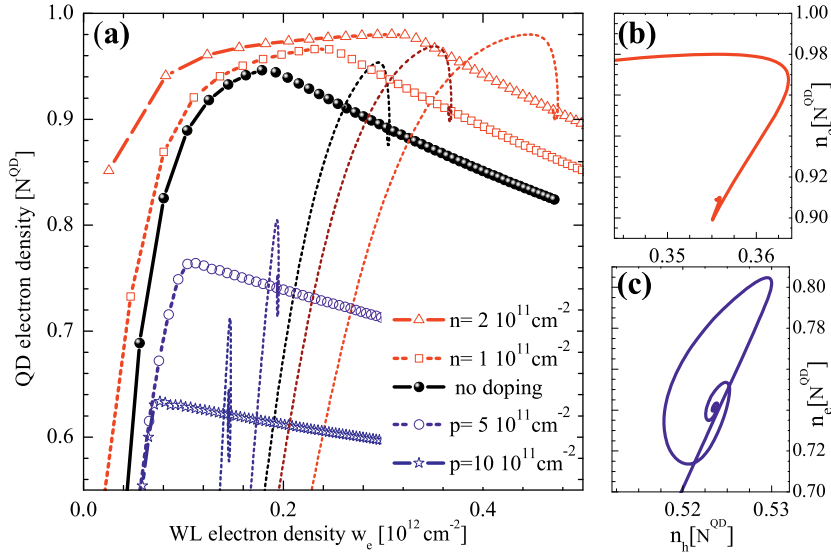
Fig. 7. (Color online) Effect of WL doping: steady state characteristic for a range $j = 0$ to $j/e_0 = 2 \times 10^9$ cm^{-2} (symbols) and turn-on trajectories for $j = 2.5\,j_{th}$ (lines) projected onto the (w_e, n_e)-phase space (a) squares, triangles, circles and stars are doping densities of $n = 1 \times 10^{11}$ cm^{-2}, $n = 2 \times 10^{11}$ cm^{-2}, $p = 5 \times 10^{11}$ cm^{-2}, and $p = 10 \times 10^{11}$ cm^{-2}, respectively; (b) and (c): turn-on trajectory projected onto the (n_h, n_e)-phase space for $n = 2 \times 10^{11}$ cm^{-2} and $p = 5 \times 10^{11}$ cm^{-2}, respectively. Parameters as in Table 1.
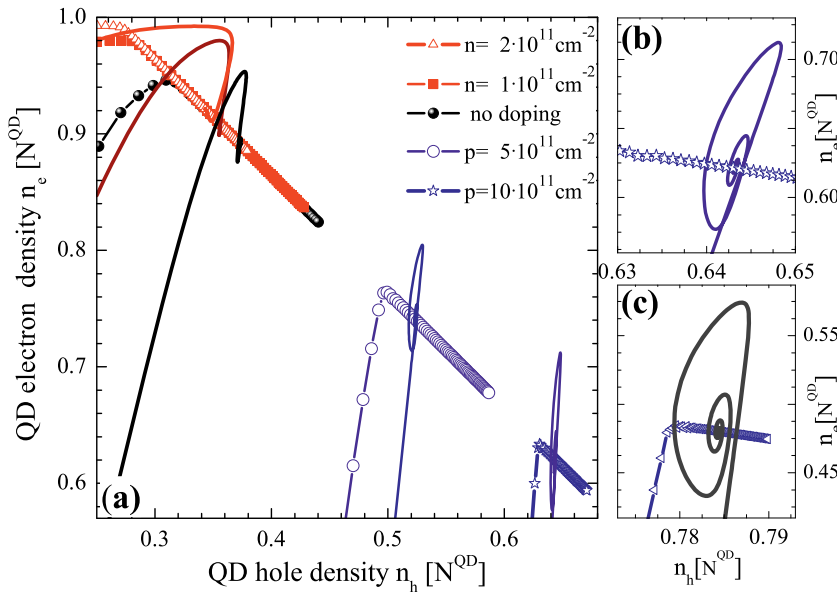
Fig. 8. (Color online) Effect of WL doping: steady state characteristic for a range $j = 0$ to $j/e_0 = 2 \times 10^9$ cm^{-2} (symbols) and turn-on trajectories for $j = 2.5\,j_{th}$ (lines) projected onto the (n_h, n_e)-phase space (a) squares, triangles, circles and stars are doping densities of $n = 1 \times 10^{11}$ cm^{-2}, $n = 2 \times 10^{11}$ cm^{-2}, $p = 5 \times 10^{11}$ cm^{-2}, and $p = 10 \times 10^{11}$ cm^{-2}, respectively; (b) and (c): close-up of (a) for $p = 10 \times 10^{11}$ cm^{-2} and $p = 20 \times 10^{11}$ cm^{-2}, respectively. Parameters as in Table 1.

decreases both densities. The reason is that the n-doping increases the WL electron density which then leads to higher in-scattering rates S_e^{in} (see Fig. 2a) and therefore to higher n_e^*. On the contrary, p-doping leads to a higher WL hole concentration and thus to higher occupation of the QD hole levels. Note, however, that the increased WL hole density for p-doped samples also has an effect on the out-scattering rate, as this contains a factor that exponentially decreases with w_e through the detailed balance relation (Eq. (8)). The scattering time τ_h for holes decreases with increasing p-doping while the scattering time for electrons increases. The ratio between the timescales of both carriers decreases from $\tau_h/\tau_e = 5/100$ for the undoped case to a value of $\tau_h/\tau_e = 3/500$ for a p-doping of $p = 20 \times 10^{11}$ cm^{-2} thus explaining the lower damping (see discussion in Sect. 3.1). Figures 7b and 7c show the turn-on dynamics in the (n_h, n_e)-phase space for the extreme cases of n- and p-doping, corresponding to very strongly and weakly damped relaxation oscillations, respectively (for n-doping $n = 2 \times 10^{11}$ cm^{-2} the ratio between the timescales is $\tau_h/\tau_e = 5/30$).

Figure 8a shows the steady state characteristics discussed in Figure 7a projected onto the (n_h, n_e)-phase space for 2 different n-doping densities (red squares and triangles) and 2 different p-doping densities (blue circles and asterisks). Figure 8b, 8c shows close-ups for very high p-doping. Going from high p-doping to n-doping the steady states n_e^* and n_h^* move up along an approximately straight line in (n_h, n_e)-phase space, while the turn-on dynamics becomes more strongly damped and synchronized between electrons and holes. This is different to changing the steady state values by varying the confinement energy as there increased steady state values n_e^* (induced by increasing ΔE_e) lead to a desynchronization (separation of timescales) of electrons and holes.

Figure 9 shows the steady state characteristics and turn-on dynamics in (w_h, n_h)-phase space, illustrating the increased QD and WL hole densities for p-doping.

5 Conclusion

In conclusion, we have found that the details of the energy scheme of the QD-WL system sensitively influence the microscopically calculated nonlinear scattering rates, and hence the nonlinear turn-on dynamics. We have systematically studied the effects of the electron and hole confinement energies and zero-point energies as well as the doping of the wetting layer. The dynamics of electrons and holes becomes the more synchronized the more similar the scattering times are. We have shown that the inclusion of separate dynamics of holes and electrons is crucial in order to explain the dynamic behavior of a QD laser with a doped wetting layer. Introducing p-doping drastically reduces the damping of the turn-on relaxation oscillations which is a significant feature influencing the modulation response of these QD lasers. On the other hand, n-doping increases the damping.
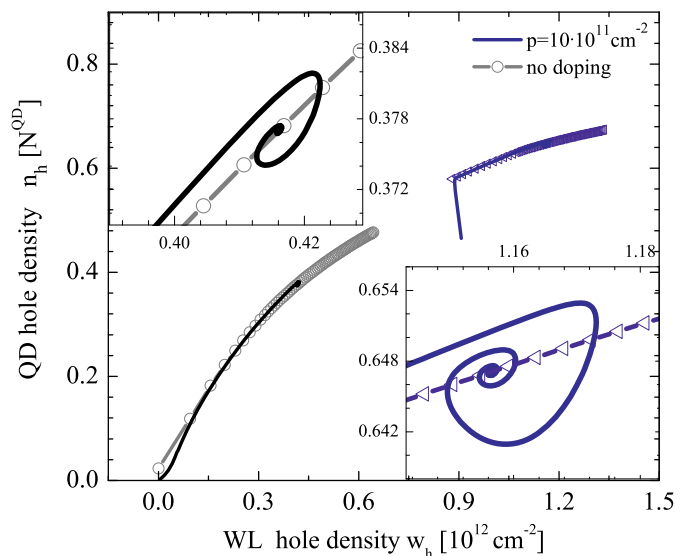
Fig. 9. (Color online) Steady state characteristics for a range $j = 0$ to $j/e_0 = 2 \times 10^9$ cm^{-2} (symbols) and turn-on trajectories for $j = 2.5\, j_{th}$ (lines) projected onto the (w_h, n_h)-phase space for undoped (black) and p-doped WL with $p = 10 \times 10^{11}$ cm^{-2} (blue). Insets show enlargements around the steady state for $j = 2.5\, j_{th}$. Parameters as in Table 1.

References

1. D. Bimberg, M. Grundmann, N.N. Ledentsov, *Quantum Dot Heterostructures* (John Wiley & Sons Ltd., New York, 1999)
2. W.W. Chow, S.W. Koch, *Semiconductor-Laser Fundamentals* (Springer, Berlin, 2004)
3. J. Kim, S.L. Chuang, IEEE J. Quantum Electron. **42**, 942 (2006)
4. E. Malić, K.J. Ahn, M.J.P. Bormann, P. Hövel, E. Schöll, A. Knorr, M. Kuntz, D. Bimberg, Appl. Phys. Lett. **89**, 101107 (2006)
5. E. Malić, M.J.P. Bormann, P. Hövel, M. Kuntz, D. Bimberg, A. Knorr, E. Schöll, IEEE J. Sel. Top. Quantum Electron. **13**, 1242 (2007)
6. K. Lüdge, M.J.P. Bormann, E. Malić, P. Hövel, M. Kuntz, D. Bimberg, A. Knorr, E. Schöll, Phys. Rev. B **78**, 035316 (2008)
7. K. Lüdge, E. Schöll, IEEE J. Quantum Electron. **45**, 1396 (2009)
8. T.R. Nielsen, P. Gartner, F. Jahnke, Phys. Rev. B **69**, 235314 (2004)
9. C. Otto, K. Lüdge, E. Schöll, Phys. Stat. Sol. B **247**, 829 (2010)
10. D.G. Deppe, H. Huang, IEEE J. Quantum Electron. **42**, 324 (2006)
11. K. Veselinov, F. Grillot, C. Cornet, J. Even, A. Bekiarski, M. Gioannini, S. Loualiche, IEEE J. Quantum Electron. **43**, 810 (2007)
12. M. Gioannini, I. Montrosset, IEEE J. Quantum Electron. **43**, 941 (2007)

13. T. Erneux, E.A. Viktorov, P. Mandel, Phys. Rev. A **76**, 023819 (2007)

14. A. Fiore, A. Markus, IEEE J. Quantum Electron. **43**, 287 (2007)

15. A.E. Viktorov, P. Mandel, A.G. Vladimirov, U. Bandelow, Appl. Phys. Lett. **88**, 201102 (2006)

16. M. Lorke, F. Jahnke, W.W. Chow, Appl. Phys. Lett. **90**, 051112 (2007)

17. H.C. Schneider, W.W. Chow, S.W. Koch, Phys. Rev. B **70**, 235308 (2004)

18. W.W. Chow, S.W. Koch, IEEE J. Quantum Electron. **41**, 495 (2005)

19. J. Gomis-Bresco, S. Dommers, V.V. Temnov, U. Woggon, M. Lämmlin, D. Bimberg, E. Malić, M. Richter, E. Schöll, A. Knorr, Phys. Rev. Lett. **101**, 256803 (2008)

20. D. O'Brien, S.P. Hegarty, G. Huyet, A.V. Uskov, Opt. Lett. **29**, 1072 (2004)

21. H. Dery, G. Eisenstein, IEEE J. Quantum. Electron. **41**, 26 (2005)

22. E. Gehrig, O. Hess, Phys. Rev. A **65**, 033804 (2002)

23. C. Xing, E.A. Avrutin, J. Appl. Phys. **97**, 104301 (2005)

24. G. Lasher, F. Stern, Phys. Rev. **133**, A553 (1964)

25. J. Kim, M. Laemmlin, C. Meuer, D. Bimberg, G. Eisenstein, IEEE J. Quantum Electron. **45**, 240 (2009)